Effects of faults on vapor transport in convection surrounding a heated repository in an unsaturated formation.

by

O.M. Phillips
Department of Earth & Planetary Sciences
The Johns Hopkins University
Baltimore, MD 21218

Summary

The extent to which a fault can modify air flow patterns in an unsaturated, fractured medium is shown to be indexed by the Fault Flow Number, F, a dimensionless combination of the fault permeability, matrix permeability and formation thickness. When $F \ll 1$, the presence of the fault has little or no effect, but when $F \gg 1$, the fault plane acts as a free surface for flow in the formation. In convective gas flow surrounding a sub-boiling heated repository, a simple two-dimensional numerical model shows that the pattern of gas flow is significantly affected by the fault when $F > 3$ or so, with vertical flow short-circuited by the fault. When $F > 10$, as much as 85% of the convective circulation is vented into the atmosphere via the fault, concentrating in the fault plane the condensation of liquid water from vapor which occurs above the repository. Consideration is extended to the three-dimensional flow situation when a fault transects a repository of finite horizontal extent. If $F \gg 1$, the flow is dominated by circulation in the fault plane itself, with volume transports and condensation rates greater than in the two-dimensional case by factors of order F.

9506160071 950419
PDR WASTE
WM-11 PDR

1. Introduction

The proposed high level radioactive waste repository in Yucca Mountain, Nevada, is projected to be located at a depth of about 350 m, some 225 m above the water table, in the Topopah Spring welded tuff. This rock is generally described (Klavetter and Peters, 1986) as having a very low matrix permeability ($10^{-18} m^2$), low-to-medium matrix porosity (~0.1) and a high density of fractures (> 10 per meter). It is, however, becoming apparent (Buscheck et al, 1992) that the meso-scale hydrological behaviour is dominated not by the highly impermeable matrix but by the dense pattern of fractures which appear to be ubiquitous, though their spatial density, orientations and effective apertures vary considerably. In situ permeability measurements made by Lee and Ueng (Ramirez 1991) over 36 cm intervals in a 5 m length of a borehole gave values that scattered widely between 10^{-10} and $10^{-12} m^2$. The larger values were strongly associated with local fracture density - the authors were, in fact, unable to measure the largest values of permeability at several locations where highly fractured zones were present. Clearly the fractures provide the pathways for fluid flow, since the permeability of the fracture network is at least six orders of magnitude larger than that of the unfractured rock. The porosity provided by the fracture system is, however, very small, of order $(1 \text{ to } 6) \times 10^{-3}$ compared with that of the rock, about $0 \cdot 1$. Although the fractures provide the pathways for fluid flow, the matrix blocks provide the reservoirs. On scales large compared with the fracture spacing yet small compared with the formation thickness, in steady flow conditions the medium may (with care) be regarded as a continuum, either in the simple Darcy sense or as a dual continuum, as envisioned by Barenblatt et al (1960).

The Yucca mountain site is also traversed by several fault zones, notably the Sundance and Ghost Dance Fault Systems (Spengler, Braun, Martin and Weisenberg, 1994) (Scott and Bonk, 1984) which intersect the proposed repository location. The major fault zones in Yucca mountain have lateral extents of kilometers while individual extension and shear fractures may be only a few meters long, but the distinction between macroscopic faults and microscopic fractures is not only one of scale. The blocks of the formation on either side of a fault have experienced relative displacements that may be tens or hundreds of meters, often juxtaposing layers of considerably different hydrological properties. The spacing between faults is generally on a scale of tens of meters to kilometers, so that the existence of the discontinuity must be taken specifically into account, not smoothed or locally averaged as one sometimes can with a network of small-scale fractures, as mentioned above.

The hydrologic characteristics of faults can vary considerably and are generally poorly understood. Professor L.A. Hardie (personal communication) has pointed out that springs are frequently associated with faults, indicating the occurrence of preferred fluid pathways in the fault zone. Dudley and Larson (1976) demonstrate clearly the occurrence of springs along faults in a considerable number of instances in the Amargosa Valley, south of Yucca mountain. Though of course there must be areas of contact, the fault may contain a network of channels of varying aperture, partly or wholly filled with detritus ground from the rocks on either side during their relative displacement. As Sibson (1986) has pointed out, jogs in a fault plane are frequently the sites of brecciation and cavity formation. All of these allow flow along the fault that can redistribute the matrix or fracture/matrix flows in the rock bodies on either side. The extent of this redistribution will be shown below to be indexed by a dimensionless parameter, the fault flow number F,

formed from the fault plane permeability, the overall bulk permeability of the rock fabric and formation thickness. Because of the largely unknown and potential variability of these properties, the fault flow number may vary over many orders of magnitude. It will, however, be shown that as far as overall patterns of flow (and condensation/evaporation in gas flow in an unsatured formation) are concerned, there are two useful limiting cases that generally simplify and aid understanding. When $F < 0.3$ or so, the gas flow in the fault is a negligible part of the overall pattern and may often be ignored. When $F > 3$ or so, the fault offers such a relatively free path to flow that it acts essentially as a free surface to the blocks on either side; flow patterns on either side are essentially independent and can be estimated or calculated separately. Only for $0.3 \lesssim F \lesssim 3$ does a numerical model require coupling conditions across the discontinuity (which present numerical codes are ill-suited to provide). It is clearly important that field measurements establish the order of magnitude of this parameter for the Yucca Mountain faults, so that the qualitative nature of the flow and condensation/evaporation patterns surrounding the repository can be established.

When F is large, both gas flow and condensation of water vapor above the repository will be shown to be concentrated along the fault, by as much as 85% of the whole. Initially, in the very early stages of repository operation, the condensation would be imbibed into the unsaturated matrix on either side of the fault, but as the repository temperature increases, the gas flow rate and condensation rate increase proportionately while the increasing saturation of the rock on either side of the fault reduces the imbibition rate. The questions of whether, after what time and at what rate liquid water will begin to dribble down the fault to repository depths will be addressed in later research.

The main purpose of this paper is to provide insight into the first order effects of faults traversing the geological formations in the vicinity of a sub-boiling repository heat source. We seek qualitative understanding of how the flow and condensation patterns are modified by a fault, rather than detailed numerical precision (possibly illusory anyway because of the parameter uncertainties involved). We therefore consider convective two-dimensional gas flow in a rectangular region surrounding an internal heat source representing the repository, and study, for a range of fault flow numbers F and fault locations, the variations in these patterns, to obtain simple and robust statements applicable to field situations.

2. The Fault Plane Permeability and Fault Flow Number

Since our primary interest is in qualitative features of the flow pattern, we adopt the Boussinesq approximation, in which variations in fluid density are neglected except insofar as they influence the buoyancy. In this approximation, the interstitial fluid is regarded as incompressible so that the velocity field is divergence-free, the variations in gas density influencing only the buoyancy. This requires that the overall temperature differences ΔT be a small fraction of the absolute temperature and that the gas temperature be not near the boiling point of water, so that the density of vapor in the gas varies linearly with temperature.

The fluid buoyancy that drives the convective flow is produced by a temperature contrast ΔT between the repository surfaces and the ambient (undisturbed) matrix, and this provides a possible temperature scale. The formation thickness h provides a length scale. The balance among buoyancy, pressure gradient and viscous flow resistance represented by Darcy's equation gives scales for the magnitude of the transport velocity and (non-hydrostatic) pressure variations as

$$\frac{g\beta k(\Delta T)}{\nu} \quad \text{and} \quad \rho_g g\beta h(\Delta T) \tag{2.1}$$

respectively, (Phillips, 1991) where β is the volumetric expansion coefficient, k the matrix permeability and ν the kinematic viscosity of the gas. Note, however, that in the present application, this temperature contrast initially increases as the repository heats up, and the convective transport velocity increases proportionately. It is more convenient in considering the evolution of the thermohydrology to use a fixed temperature (and velocity) scale so that ΔT will be defined as the temperature difference between repository and upper free surface under steady conditions with a uniform, steady heat output from the source. The dimensionless form of Darcy's equation is then

$$\underset{\sim}{u} = -(\nabla p - \theta \underset{\sim}{l}) \tag{2.2}$$

where the velocity and pressure are scaled using (2.1), length by $h.\theta = T/\Delta T$ and $\underset{\sim}{l}$ is a unit vector vertically up.

In an unsaturated, highly fractured medium, the liquid water, confined by capillarity to the matrix blocks, is essentially immobile and the slowly evolving temperature field is specified by the heat balance for the medium:

$$(\rho C)_m \frac{\partial T}{\partial t} + (\rho C)_g \underset{\sim}{u}' \cdot \nabla T = K_m \nabla^2 T$$

where $(\rho C)_m$ is the product of density and specific heat for the matrix and $(\rho C)_g$ that for the gas, while $\underset{\sim}{u}'$ is the dimensional transport velocity and K_m is the matrix thermal conductivity. Latent heat of evaporation or condensation would be represented by a heat sink or source on the right of this equation, but it is shown in §3 that this is usually unimportant in the

fracture-matrix medium, and so will be neglected here. The thermal time scale is h^2/α where $\alpha = K_m/(\rho C)_m$ is the thermal diffusivity and the dimensionless form of this equation is

$$\frac{\partial\theta}{\partial\tau} + \frac{(\rho C)_g}{(\rho C)_m} Ra \; \underline{u}\cdot\nabla\theta = \nabla^2\theta \tag{2.3}$$

where $\tau = t\alpha/h^2$ and

$$Ra = \frac{g\beta(\Delta T)kh}{\nu\alpha} \tag{2.4}$$

is the Rayleigh-Darcy number. In this context, it can be interpreted as the ratio of the thermal diffusion time h^2/α to the flow-through time of the <u>transport</u> velocity field (2.1) (not of the fluid elements), i.e.

$$h\left(\frac{g\beta k(\Delta T)}{\nu}\right)^{-1} \tag{2.5}$$

In interstitial <u>water</u> flow, the Rayleigh-Darcy number is an index of the ratio of heat transfer by advection to diffusion, but the additional factor $(\rho C)_g/(\rho C)_m < 10^{-3}$ in (2.3) means that heat advection by gas flow is always negligible in this context compared with conduction. (With matrix permeability k in the range 10^{-15} to $10^{-11} m^2$, Ra is in the range 10^{-2} to 10^2). Accordingly, the center term in (2.3) is negligible and the equation simplifies to

$$\frac{\partial\theta}{\partial\tau} = \nabla^2\theta \tag{2.6}$$

Boundary conditions and juncture conditions across fault discontinuities are needed to complete the specification. At an impermeable boundary, there is no flow across it so that

$$\underline{u}\cdot\underline{n} = 0 \tag{2.7}$$

At a free surface (to the atmosphere for example) the gas pressure just inside the boundary equals that outside which can be taken as constant. There is no (non-hydrostatic) pressure gradient along the free boundary, so that fluid flows across it, either into or out of the rock, in the direction normal to it.

A fault traversing the formation represents a physical discontinuity across which juncture conditions connect the flow regimes on either side. The width of a fault is generally very small on a formation scale and the gas pressure varies very little across the fault gap, even if it is filled with detritus, so that the gas pressures in the rock medium on either side of the fault must be equal:

$$p_1 = p_2 \tag{2.8}$$

where *1* and *2* represent the regions on the two sides. Gas may, of course, enter and leave the fault as well as flow along it. If $\underset{\sim}{q}$ represents the (two-dimensional) gas volume flux in the fault plane, the integral of the gas velocity across the gap, then mass conservation gives

$$\nabla \cdot \underset{\sim}{q} = - (\underset{\sim}{u}_1 \cdot \underset{\sim}{n}_1 + \underset{\sim}{u}_2 \cdot \underset{\sim}{n}_2) \tag{2.9}$$

where $\underset{\sim}{n}_1$ and $\underset{\sim}{n}_2$ are unit normals on the two sides, each pointing away from the fault.

If the gas flow in the fault gap is at low Reynolds number $Re = q/\nu$, the volume flux per unit breadth q is a linear function of the sum of the non-hydrostatic pressure gradient and the buoyancy force, as is the velocity in Darcy's equation. Accordingly, the volume flux can be expressed in terms of a fault plane permeability κ_f defined analogously to the usual matrix perme-

ability as a geometrical constant of proportionality connecting the volume flux $\underset{\sim}{q}'$ to the driving force. In the absence of buoyancy effects, the driving force is the (non-hydrostatic) pressure gradient and

$$\underset{\sim}{q} = -\frac{\kappa_f}{\nu}\nabla_s p,$$

where ∇_s is the gradient in the plane of the fault. If temperature variations are significant, then

$$\underset{\sim}{q}' = -\frac{\kappa_f}{\mu}(\nabla_s p - \rho_0 g\beta T \sin\psi \underset{\sim}{s}) \tag{2.10}$$

where $\underset{\sim}{s}$ is a unit vector in the plane of the fault, upslope and ψ is the angle of dip of the fault. Note that $\underset{\sim}{q}$ has the physical dimensions $UL(m^2s^{-1})$ and κ_f has units L^3 or m^3. If the fault gap is open, with width δ, then $\kappa_f \approx \overline{\delta^3}/24$; if it is filled with detritus with permeability k_f, $\kappa_f \sim k_f\delta$. The fault plane permeability appears to be an important hydrological quantity in this context, and, unfortunately, a difficult one to measure in the field.

The first juncture condition (2.8) can be expressed in terms of the flow field by use of (2.10). Since (2.8) holds at all points on the fault, the pressure gradients in the interstitial fluid in directions along the fault are the same on either side and equal to the pressure gradient of the gas <u>in</u> the fault. Moreover, there is no discontinuity in temperature across the fault so that the term in the bracket of (2.10) is continuous across it. Thus

$$\frac{\underset{\sim}{q}'}{\kappa_f} = \frac{\underset{\sim}{u}'_1}{k_1} = \frac{\underset{\sim}{u}'_2}{k_2} \tag{2.11}$$

in terms of dimensional quantities. If the rock permeabilities on either side of the fault are the same, so are the transport velocity components parallel

to the fault. The scale velocity is $g\beta k(\Delta T)/\nu$ as given in (2.1), so that the scale for volume flux in the fault is $g\beta k(\Delta T)h/\nu$, the flow along it being of the order of the product of the transport velocity entering it times its length. When $k_1 = k_2 = k$, in dimensionless terms, (2.11) becomes

$$\underset{\sim}{q} = F\underset{\sim}{u}_1 = F\underset{\sim}{u}_2 \tag{2.12}$$

where the velocities represent components parallel to the discontinuity and the ratio

$$F = \frac{\kappa_f}{kh} \tag{2.13}$$

will be called the Fault flow number.

The magnitude of this parameter will be found to have a strong influence on the pattern of gas flow in the formation. There seems to be no information on what its magnitude might be at the Yucca mountain site because of the uncertainties in k (by a factor 10^4) and ignorance of κ_f. Table 1 illustrates a range of possibilities - with $h = 500$ m conceivable values of F range from very large to very small. What are the flow characteristics in these two limits? Over what range of F does the flow pattern shift from one type to the other?

The first question can be answered by consideration of (2.12). Recall that the dimensionless quantities are O(1) - they may happen to be small in some regions but they cannot be numerically large. When the fault flow number $F \ll 1$ since $\underset{\sim}{u}_1 = \underset{\sim}{u}_2 = O(1)$, $q \ll 1$; gas flow along the fracture is very small. When $q \ll 1$, the two terms on the right of (2.9) must balance which means that

the normal as well as the tangential velocities in the matrix are continuous across the fault, as they would be if the fault were not there. When $F \ll 1$, then, the fault has very little influence on the flow.

$(\bar{\delta}^3)^{1/3}$ (m)	κ_f (m)	$k(m^2)$ 10^{-15}	10^{-14}	10^{-13}	10^{-12}	10^{-11}
10^{-4}	4.10^{-14}	8.10^{-2}	8.10^{-3}	8.10^{-4}	8.10^{-5}	8.10^{-6}
3.10^{-4}	10^{-12}	2	0.2	2.10^{-2}	2.10^{-3}	2.10^{-4}
10^{-3}	4.10^{-11}	80	8	0.8	8.10^{-2}	8.10^{-3}
3.10^{-3}	10^{-9}	2.10^{3}	2.10^{2}	20	2	0.2
10^{-2}	4.10^{-8}	8.10^{4}	8.10^{3}	8.10^{2}	0.8	8

Table 1. Values of the fault flow number $F = \kappa_f / kh$ for various matrix permeabilities and equivalent fault gaps δ for a formation of thickness h = 500 m.

On the other hand, when the fault flow number is large, $F \gg 1$, and since $q = O(1)$ the tangential velocities $\underset{\sim}{u}$ and $\underset{\sim}{u}_2$ must be very small. Interstitial gas flow enters or leaves the fault in the directions perpendicular to it - this is the free surface condition as at the upper (atmospheric) boundary surface. When $F \gg 1$, then, the fault permeability is so large and the pressure gradient along it so small that the fault acts in essence as a free surface for the gas flow, the flow pattern on each side being driven by the temperature distribution internal to the block on that side, and being independent of the flow and temperature distributions in the other. Either of

these limits allows a considerable simplification in numerical computation of the formation flows; the question of how large or how small F must be will be explored in a simple model.

3. Dimensionless Equations and Scales

For the numerical model, consider the rectangular region shown in Figure 1 with the upper surface open to gas flow and the others impermeable, the region being initially at uniform temperature but then heated internally at a constant rate Q per unit area by a heat source at mid-depth over the middle third of the region. A superimposed vertical geothermal gradient does not modify the flow; as equation (3.4) below demonstrates, the streamfunction is determined by the horizontal temperature gradient. The boundaries are taken at constant temperature (zero) and as time progresses, the repository temperature increases and heat diffuses outwards. The temperature scale ΔT is chosen so that a steady heat flux upwards to the surface $\left(\frac{1}{2}Q\right)$ is associated with a temperature difference ΔT across the distance $\frac{1}{2}h$, i.e.

$$\Delta T = \frac{Qh}{4\alpha} \tag{3.1}$$

where α is the thermal diffusivity.

The most convenient time scale for calculation is simply h^2/α, as in (2.3). This time scale is, however, numerically large compared with the time interval over which the thermal field approaches an approximately steady state. If we define this, t_s, as the time over which the total heat output, Qt_s, is equal to the steady state heat content, $\frac{1}{2}(\Delta T)h$, then from (3.1)

$$t_s = \frac{h^2}{8\alpha} \tag{3.2}$$

The evolution of the temperature field is specified by (2.6)

$$\theta_\tau = \theta_{xx} + \theta_{zz}$$

with $\theta = 0$ on the outer boundaries and

$$\frac{\partial\theta}{\partial z} = \pm\frac{1}{2}$$

on the lower and upper surfaces of the repository at $z = \frac{1}{2}$.

The lower boundary condition, $\theta = 0$, is perhaps not very realistic as a representation of conditions at the water table below a repository, since the specific heat of the saturated rock is not significantly larger than unsaturated rock. The lower boundary temperature would be expected to rise, reducing the temperature gradient below the repository and so the heat flux directed downwards. This would somewhat increase the repository temperature and the heat flux upwards, but the temperature field would not be qualitatively different. Also, the horizontal extent of the model is rather limited. A test calculation showed that if it was extended, the streamlines were somewhat more diffuse at the edges, in regions where evaporation is very small.

The gas flow field induced by the temperature distribution can be considered incompressible, and in two dimensions a (dimensionless) stream function ψ can be defined such that

$$u = -\frac{\partial\psi}{\partial z}, \qquad w = \frac{\partial\psi}{\partial x}, \tag{3.3}$$

the z-axis being vertically upwards. The pressure can be eliminated from (2.2) by cross-differentiation of the component equations, and this leads to

$$\psi_{xx} + \psi_{zz} = \theta_x \tag{3.4}$$

where the units of streamfunction are $g\beta(\Delta T)kh/\nu$. Recall that the differences in the value of the streamfunction at two points is the volume flux across a line joining them, so that the units of ψ and q are the same.

The boundary conditions on the flow are that ψ = const. on impermeable boundaries, $\partial\psi/\partial n = 0$ on free boundaries (such as the upper surface) and, from (2.12), at a fault separating blocks 1 and 2,

$$q = \psi_2 - \psi_1 = F\frac{\partial\psi}{\partial n}\Big|_1 = F\frac{\partial\psi}{\partial n}\Big|_2 \tag{3.5}$$

where the unit normal is directed from 1 to 2. Since the definition (3.3) satisfied incompressibility, the juncture condition (2.9) is satisfied automatically.

Before the flow patterns are described, it is useful to recall the physical and geometrical interpretations of the governing equations (2.2), (3.4) and (3.5). In (2.2), let us integrate the equation along a streamline (flow path) either from the point where it enters the region from the atmosphere to the point where it leaves it, or, in the case of a closed streamline, right around the path.

$$\int \underline{u}\cdot d\underline{S} = -\int \nabla p\cdot d\underline{S} + \int \theta dz$$

since l is a vertical unit vector and $d\underline{S}\cdot\underline{l} = dz$. The pressure integral vanishes since the two ends of the circuit have the same pressure and we have

$$\int \underline{u}\cdot d\underline{S} = \int \theta dz$$

or, in words,

(*transport flow speed*) x (*path length*) ~ (*temperature rise*) x (*depth of heated region*).

Consequently,

$$\textit{transport flow speed} \sim \frac{(\textit{temperature rise})\times(\textit{depth of heated path})}{(\textit{path length})} \tag{3.6}$$

Thus, if a highly permeable fault ($F \gg 1$) intersects the flow and reduces the path length by, say, 50%, the transport flow speed in the matrix is approximately doubled.

Another useful interpretation follows from (3.4). Contours ψ = const. are streamlines. Maxima in ψ are surrounded by closed contours ψ = const. (as are geographic maxima) with $\nabla^2\psi = \psi_{xx} + \psi_{zz} < 0$. This is associated with a clockwise circulation and, from (3.4), with $\theta_x < 0$, temperature <u>decreasing</u> as we move to the right. Conversely, when the temperature increases to the right, $\theta_x > 0$, circulation is counter-clockwise and ψ is a minimum. The major features of the velocity pattern can then be interpreted simply and immediately in terms of the temperature pattern.

Finally, in (3.5), if the fault flow number $F \ll 1$, $\psi_1 = \psi_2$, the streamlines are continuous across the fault. If $F \gg 1$, $\partial\psi/\partial n$ is very small on either side and the streamlines are normal to the fault as they are in the free surface. Fluid flow along the fault may be substantial.

We now turn to the distributions of evaporation and condensation. The balance equation for water vapor density can be written as

$$\frac{\partial}{\partial t}(S_g \phi \rho_v) + \nabla\cdot(\rho_v \underline{u}') = \nabla\cdot(D\nabla\rho_v) - \Gamma_v \tag{3.7}$$

where S_g is the gas saturation, ϕ the bulk porosity, ρ_v the water vapor density, D the vapor diffusivity in air in the fracture/matrix system, allowing for porosity, tortuosity, etc., and Γ_v is the mass of vapor per unit matrix volume condensed as liquid water per unit time. If evaporable water is present, it is generally supposed that the vapor pressure and density are

close to saturation at the ambient temperature and (3.7) becomes a recipe for Γ_v, the distribution of condensation rate. Since in slowly varying temperature fields the vapor storage time derivative term can be neglected,

$$\Gamma_v = - \underline{u}' \cdot \nabla \rho_v + D \nabla^2 \rho_v \tag{3.8}$$

in which spatial variations in D are ignored. Now

$$\rho_v = \rho_v(T) \approx \rho_v(T_o) \exp\left\{ -\frac{L M_w}{R} \left(\frac{1}{T} - \frac{1}{T_o} \right) \right\} \tag{3.9}$$

according to Claperyon's equation (see, e.g. Wark, 1983), where L is the enthalpy change on evaporation, M_w the molecular weight and R the gas constant. In virtue of (3.9)

$$\begin{aligned} \Gamma_v &= - \left(\frac{\partial \rho_v}{\partial T} \right) \underline{u}' \cdot \nabla T + D \left\{ \frac{\partial^2 \rho_v}{\partial T^2} (\nabla T)^2 + \frac{\partial \rho_v}{\partial T} \nabla^2 T \right\} \\ &\approx - \left(\frac{\partial \rho_v}{\partial T} \right) \underline{u}' \cdot \nabla T + \frac{D}{\rho_v} \left(\frac{\partial \rho_v}{\partial T} \right)^2 (\nabla T)^2 \end{aligned} \tag{3.10}$$

with use of (3.9).

A convenient scale for the condensation rate Γ_v is such that this rate of condensation produces an order unity liquid saturation in the matrix within an internally defined time scale. One possible time scale that could be used is the flow-through time scale for fluid elements in the gas flow, $\phi h / u_s$, where u_s is the transport speed scale (2.1). Based on this convective scale, the dimensionless condensation rate

$$\hat{\Gamma}_c = \frac{\Gamma_v}{\phi \rho_l} \left(\frac{\phi h}{u_s} \right) \tag{3.11}$$

where ρ_l is the <u>liquid</u> density, and

$$\hat{\Gamma}_c = - F_1(T) \underline{u} \cdot \nabla \theta + F_2(T) Pe^{-1} (\nabla \theta)^2 \tag{3.12}$$

where the Peclet number $Pe = u_s h/D$ is proportional to the gas flow Rayleigh number and $F_1(T)$ and $F_2(T)$ are dimensionless functions of the temperature:

$$F_1(T) = \frac{\Delta T}{\rho_l}\left(\frac{\partial \rho_v}{\partial T}\right), \qquad F_2(T) = \frac{\rho_l}{\rho_v}\{F_1(T)\}^2 \tag{3.13}$$

The function $F_1(T)$ (shown in Figure 2) is (ρ_v/ρ_l) times the 'vapor pressure number' defined by Manteufel and Powell (1994). With $\Delta T \sim 50°$ $F_1(T)$ is of magnitude 10^{-4} at low temperatures (30° C) and about 10^{-3} at $T \sim 90°$ C. Since $\rho_l/\rho_v \sim 10^3$, <u>both</u> F_1 and F_2 are numerically of order 10^{-3} at most. The Peclet number $Pe = (\alpha/D)Ra$ is unlikely to be smaller than 10^{-2}. Consequently, since the dimensionless flow functions in (3.12) are of order unity (they turn out to be in fact numerically rather small), water condensation or evaporation in the bulk of the region apparently produces at most a 10% change in liquid saturation in the flow-through time $\phi h/u_s$.

However, the uncertainty in the effective overall permeability (by some four orders of magnitude) results in an equal uncertainty range in the flow-through time. Though it only shifts the uncertainty, it is probably better to use as a time scale, the thermal diffusion time to approach equilibrium, $t_s = h^2/8\alpha$. For Yucca mountain, with $\alpha = h \sim 550m$, $t \sim 1{,}700$ yr. The dimensionless condensation rate, i.e. that required to produce an $O(1)$ change in liquid saturation in the diffusion time interval t_s is then

$$\hat{\Gamma}_d = \frac{\Gamma_v}{\phi \rho_l}\left(\frac{h^2}{8\alpha}\right) \tag{3.14}$$

and, from (3.10)

$$\hat{\Gamma}_d = -\left\{\frac{F_1(T)Ra}{8\phi}\right\}\underline{u}\cdot\nabla\theta + \left\{\frac{F_2(T)D}{8\alpha\phi}\right\}(\nabla\theta)^2 \tag{3.15}$$

Since the maximum probable value of Ra is of order 200, and $\phi \sim 0.1$ for the medium, the coefficient in the first term in 0.2 at most. The function F_2 is also of order 10^{-3} and since $D/\alpha \sim 1.5$, the second coefficient is smaller, $O(10^{-3})$. Consequently, we conclude that changes in liquid saturation by evaporation/condensation in the bulk medium over the thermal diffusion time scale will also be of order 20% at most, and that when the Rayleigh number is large. Other processes, such as sporadic infiltration, may well be more important.

This analysis has neglected the thermal effects associated with liquid condensation and evaporation, represented by distributions of sources and sinks in the thermal energy balance (2.3). An *a-posteriori* justification can be given by comparing the total rate of heat deposition per unit area by condensation over the depth h, of order

$$Lh\left(\frac{\partial \rho_v}{\partial T}\right)\underline{u}\cdot\nabla T$$

(where L is the latent heat) to the heat input rate per unit area by conduction

$$(\rho C)_m \ \alpha_m \ \nabla T$$

In terms of the scales given previously, this ratio becomes

$$\left(\frac{\rho_l L}{(\rho C)_m \Delta T}\right) F_1(T) Ra$$

If $\Delta T = 80°C$, the first factor is about 7, $F_1(T) \sim 10^{-3}$ and $Ra \sim 10^2$ at most, so that as far as the fracture-matrix flow is concerned, the thermal effects of evaporation and condensation are probably negligible but may be significant if the permeability and gas flow Rayleigh number are both large.

This conclusion holds also for phase changes in a fault with $F \gg 1$ that vents interstitial gas flow. The volume flux per unit length of the fault is of order uh, so that the equivalent heat source or sink per unit area of fault is as given above, generally small compared with that represented by the repository.

However, it will be found below that when the fault flow number $F \gg 1$ and the fault intersects the repository heat source, most of the vertical volume flow occurs in the fault, traversing the region of high temperature gradient and enhancing the vapor transport. For fault flow, (essentially in the fault plane) the significant quantity is not the volume of liquid condensed per unit volume of matrix, but the volume of liquid condensed per unit area of fault. If this is small compared with the thickness of the fault (times the porosity, if it contains detritus) then the saturation changes in the fault are small over the time interval t_s. If it is large, then liquid water must have dribbled down the fault and/or have been imbibed into the surrounding rock. Vapor diffusion along the fault plane is negligible compared with advection, so that the condensation rate in the fault flow Γ_{ff} is found by integrating (3.10) across the fault:

$$\Gamma_{ff} = -\left(\frac{\partial \rho_v}{\partial T}\right) \underset{\sim}{q}' \cdot \nabla T = -\left(\frac{\partial \rho_v}{\partial T}\right)(u_s h)\left(\frac{\Delta T}{h}\right) q \frac{\partial \theta}{\partial z}$$

where q' and q are the dimensional and dimensionless gas volume fluxes in the fault. The average volume of liquid condensate produced in unit area of the fault in the time scale $t_s = h^2/8\alpha$ is then

$$d_{ff} = \frac{\Gamma_{ff}}{\rho_l} \cdot \frac{h^2}{8\alpha} = -\frac{\Delta T}{\rho_l}\left(\frac{\partial \rho_v}{\partial T}\right)\frac{u_s h^2}{8\alpha} \; q \frac{\partial \theta}{\partial z}$$

$$= -\left(\frac{1}{8} F_1(T) Ra \cdot h\right) \; q \frac{\partial \theta}{\partial z} \qquad (3.16)$$

Thus, since $F_1(T) \sim 10^{-3}$ in a sub-boiling repository, $h \sim 550m$, and the dimensionless functions are O(1), if $Ra = 1$ $d_{ff} \sim .07m$ of water is condensed in time t_s. If $Ra = 100$. $d_{ff} \sim 7m$. These are of course averages over the fault plane - if it contains pathways or conduits along which the gas flow is further channeled, the local condensation is further enhanced.

4. Flow and Condensation Patterns.

The geometry illustrated in Figure 1 provides a simple model for calculating the effects of faults at various locations and values of the fault flow number on the overall convective flow patterns. The general magnitudes of the evaporation/condensation rates are given by the scaling analysis, and numerical integration of the dimensionless equations gives their distributions and the patterns of flow.

In the calculations, a low resolution grid (45 x 20) was used and equation (3.2) integrated forward step by step until dimensionless time 0.1. This value is based on the time scale h^2/α; in terms of the approach-to-equilibrium time, that corresponds to 0.8. The temperature distribution, which is unaffected by the fault, is shown in figure 1 in units of ΔT. At this time, the central repository temperature is 0.63 ΔT; the isotherms above and below have diffused substantially and are nearly horizontal. They slope steeply only near the ends of the repository. At earlier times, of course, the pattern is tighter and the maximum temperature smaller; at later times it is more diffuse as a steady state is approached with a maximum temperature near ΔT given by (3.1). Since these do not constitute qualitative differences, this temperature distribution was chosen to drive the convective flow fields.

In the numerical calculations for the flow fields, a simple relaxation method was used in each region, with $\psi = 0$ on the lower and side boundaries and the juncture condition (3.5) applied at the fault on each iteration. The fault was represented by two columns of numbers representing the values of the streamfunction on either side, and the normal derivatives in (3.5) were found by quadratic extrapolation from each side. Iteration was continued until convergence to 10^{-5} was achieved at all points. After some experimentation, it was found that the trends in the patterns of flow and of evaporation/condensation could be displayed most clearly using two sequences of calculation, one with a fault in a fixed location intersecting the repository, with a range of fault flow numbers F from 0.03 to 30, and the other with $F = 10$ (which provided a significant flow response) for faults in different locations relative to the repository.

The streamline patterns in the first sequence are shown in Figure 3. The location of the fault is indicated by the vertical line intersecting the repository 18 grid points from the left-hand end. In Figure 3a, $F = 0.03$ and the influence of the fault is hardly perceptible. The flow circulates around the regions of high horizontal temperature gradients (Figure 1), clockwise on the right where ψ is a maximum and counterclockwise on the left where ψ is least, with air drawn in from the atmosphere on both flanks and ejected in the central region above the heated repository. This confirms the pattern sketched qualitatively by Manteufel and Powell (1994) for repository-induced flow in the absence of faults. When $F = 0.1$, Figure 3b, flow discontinuity at the fault is beginning to become apparent as the gas, rising through the left-hand end of the repository region, begins to short-cut to the surface via the fault. This is accentuated in Figure 3c for $F = 0.3$, where the total volume transport in the left-hand gyre has increased about 25% because of the

reduction in flow resistance offered by the fault. The right-hand gyre is virtually unaffected. These three flow patterns are clearly members of the same family, with only minor differences among them - the flow pattern for $F = 0.3$ is not notably different from that when $F = 0.03$ or 0, when the fault is absent.

However, when $F = 1$, Figure 3d, major differences are apparent. The streamline dividing the two gyres has moved towards the fault, about 2/3 of the circulating flow in the left-hand gyre is drawn in from the atmosphere over the upper surface and returns to it via the fault - the remainder circulates internally. The right-hand gyre, further from the fault, has intensified somewhat (about 25%), but virtually all of the gas drawn in on the flank is returned to the atmosphere across the upper surface as when $F \ll 1$, rather than through the fault.

When $F = 3$ and larger, the new pattern consolidates. The flow still circulates around the regions of large horizontal temperature gradient near the ends of the repository. The total transports in the gyres stabilize as F increases, to about twice the volume flux when $F = 0$ in the left gyre and 25% more in the right - the fault offers negligible resistance and the circulation is limited by the resistance of the matrix in the flow in the gyres, predominantly from the atmosphere to the fault. Further increase in F will not change this flow pattern significantly since the fault is, already, when $F = 10$ to 30, acting as a free surface. The rising flow moves to the fault or the upper surface, whichever is closest.

The statement (3.6) gives a check on the magnitudes of the volume fluxes calculated. The total volume flux in a gyre is given in the computation by the maximum value of the streamfunction, about 0.04 units in figure 3a. Also,

$$\text{volume flux} \sim (\text{transport speed}) \times (\text{gyre radius})$$

$$\sim \frac{(\text{temperature rise}) \times (\text{depth of heated path}) \times (\text{gyre radius})}{(\text{path length})}$$

From Figure 1, (temperature rise) ~ 0.6, depth of heated path ~0.4 and from figure 3a, gyre radius ~ 0.5 and the flow path length ~3, giving a volume flux of order 0.04 in accordance with the value given in figure 3a. The driving buoyancy forces when $F = 30$ in figure 3g are the same, but the path length in the matrix flow is smaller by about a half in the left-hand gyre, but only somewhat smaller in the right-hand one. The volume fluxes are increased in inverse proportion.

The ability of the fault, when F is large, to attract the upwards flow is illustrated in figure 4a, which shows for various values of F, the distribution of vertical gas transport up the fault. For each value of F, this rises almost linearly from the lower boundary, reaching a maximum just above the repository level ($z/h = 0.5$). An important property to notice is that with the same thermal field driving the convection, the magnitudes of the volume fluxes increase rapidly as the fault flow number F increases beyond 1, stabilizing and becoming essentially independent of F *for* $F > 10$ or so. Figure 4b shows the percentage of the gas flow into the formation from the atmosphere that is returned to the atmosphere via this fault. At large values of F, this is as much as 85%, the remainder being in the weak inner loop surrounding the recirculating region in the right-hand gyre ($\psi = 3$ to 4.7).

Figure 5 illustrates how different locations of the fault relative to the repository heat source influence the circulations, all calculated for $F = 10$. The almost-central fault in Figure 5a short-circuits practically all of the gas flow drawn in at the flanks on either side, as it rises through the repository. The maximum volume transport in the fault is about 30% larger

than when the fault is displaced from the repository center (figures 5b or 3f). A vertical fault at the edge of the repository (Figure 5c) still has circulation on both sides, since the region of the horizontal temperature gradient extends to the left of the fault (cf Figure 1), but if the fault lies beyond this region, it short-circuits the downward flow from the atmosphere (Figure 5d) with only very weak flow beyond. In general, it is apparent that the presence of a fault with $F \gg 1$ influences the flow patterns on either side to a distance of the order of the formation thickness - the right-hand gyres of figures 3a, b and Figures 5c, d are very similar. This is, indeed, a consequence of the isotropy assumed of the medium; if the effective permeabilities K_H and K_V for horizontal and vertical flows are different, the effects are felt to a distance $(k_H/k_V)^{1/2)}$ times the formation thickness (Phillips, 1991).

The scaling analysis of the previous section has indicated that condensation and evaporation in the matrix itself associated with convection and diffusion is likely to be significant only on time scales of order a few times the thermal diffusion time. The distributions of evaporation/condensation rate from convection are shown in figure 6 for $F = 0.1$, 1 and 10; the magnitudes of $\underline{u}\cdot\nabla\theta$ are of order unity with, as one might expect, evaporation below the repository and precipitation above. For F = 10, the rates are less than at the smaller values of F since much of the upwards flow (across the isotherms) is channeled into the fault. The asymmetry of these convective distributions contrasts with the symmetric diffusive contribution (independent of Rayleigh number and fault properties) represented by the last term in equation (3.15). Contours of $(\nabla\theta)^2$ are shown in Figure 7; the maximum value is

about 4. The distributions of $q\partial\theta/\partial z$ in the fault are shown in Figure 8; note that the condensation region above the repository extends to the surface, and that it stabilizes at values of order unity when $F > 10$ or so.

5 Discussion and Conclusions

In the region surrounding a repository heat source located above the water table, the interstitial gas, air and water vapor, circulates convectively and redistributes liquid water by evaporation and condensation. When the region is transsected by one or more faults, the modification to the flow pattern in two dimensions is indexed by the fault flow number F defined in §2. The magnitudes of the fault flow numbers are, as pointed out earlier, unknown, but in the two-dimensional flow patterns considered to this point, it is sufficient to know whether they are large or small compared to unity. If F is small, a fault has little influence on the flow. If large, the fault plane or zone acts as a free surface and the convective circulation speed and pattern are again independent of F; the flow is 'choked' by its passage through the resisting medium.

However, when a fault plane transsects a finite repository region, the flow is three-dimensional and, as sketched in Figure 9, can circulate in the fault plane as well as between the fault and the medium. The distribution of volume flux across unit distance in the fault plane is specified by the analog (2.10) to the Darcy equation, so that the scale volume flux in the fault plane is

$$g\beta\kappa_f(\Delta T)/\nu \tag{5.1}$$

where κ_f is the fault plane permeability. The magnitude of the total volume flux between the fault and the medium is the velocity scale (2.10) times h, the formation thickness, and the ratio of these is again the fault flow number

(2.10): $F = \kappa_f / kh$. Thus if $F \ll 1$, a fault has again little influence on the three-dimensional circulating flow in the medium. If $F \gg 1$, however, the gas circulation is primarily in the fault plane, the total volume flux per unit distance being larger by the factor F than that which enters the fault from the matrix over the total depth h. In contrast with the two-dimensional case, the flow circulating within the fault is independent of k but proportional to κ_f and so increases proportionately to F. If the fault plane permeability is uniform, the two-dimensional patterns of flow in the fault plane are, in fact, the same as the two-dimensional patterns in the medium with no fault present, but in the volume flux units (5.1). Similarly the patterns of evaporation/precipitation in the fault plane resemble that of Figure 6a but the rates are faster than given by equation (3.15) by the factor F. Condensation occurs above the repository and one might enquire whether the rate of condensation is larger than the rate at which water can be imbibed into the fault walls, so that it seeps or runs down, presumably in the form of rillets. A corresponding question is whether the evaporation on the fault walls below the repository desiccates them to the extent that the equilibrium assumption becomes invalid. Also, does the internal energy of condensation, concentrated on the fault walls, substantially modify the temperature field in the vicinity of the fault? These questions will be the subject of future research.

The calculations have shown that modifications of the liquid saturation distribution in the matrix is a relatively slow process, significant changes occurring over time intervals long compared with the thermal equilibration time or the flow-through time. This is generally consistent with, and generalizes, the numerical calculations of Buscheck and Nitao (1992) and Pollock (1986). However, if the fault flow number should turn out to be large, the flow circulation in the fault plane or planes is much faster and the convec-

tive transports proportionately greater. Moreover, the vapor flux is concentrated in the fault zone, so that the rate of condensation above the repository is both increased and localized. The probability of liquid water reflux down the fault is thus considerably increased.

It then does seem important to measure in the field the characteristic value of the fault flow number F, and ways to do this need to be devised.

Acknowledgements

This paper documents work performed by the Center for Nuclear Waste Regulatory Analyses (CNWRA) for the US Nuclear Regulatory Commission (NRC) under contract no. NRC-02-93-005, NRC Office of Nuclear Material Safety and Safeguards, Division of High-Level Waste Management. This paper is an independent product of CNWRA and does not necessarily reflect the views or regulatory position of the NRC.

References

Buscheck, T.A. and J.J. Nitao 1992 The impact of thermal loading on repository performance at Yucca Mountain. Proc. Third Int. Conf., High Level Radioactive Waste Management, pp. 1003-1017. Amer. Nuc. Soc., 1976.

Dudley, W.W. and J.D. Larson 1976 the effect of irrigation pumping on desert pupfish habitats in Ash Meadows, Nye County, Nevada. U.S. Geol. Survey Prof. Pap. 927.

Klavetter, E.A. and R.R. Peters 1986 Estimation of hydrologic properties of an unsaturated fracture rock mass. SAND 84-2642. Sandia Nat. Lab., Albuquerque, NM.

Manteufel, R.D. and M.W. Powell 1994 Thermosyphon analysis of a repository: A simplified model for vapor flow and heat transfer. Proc. Fifth Int. Conf., High-level Radioactive Waste Management. pp. 2207-2216, Amer. Nuc. Soc.

Phillips, O.M. 1991 Flow and Reactions in Permeable Rocks. Cambridge University Press.

Pollock, D.W. 1986 Simulation of fluid flow and energy transport processes associated with High-Level Radioactive Waste disposal in unsaturated alluvium. Water Resources Res., 22, 765-775.

Ramirez, A.L. 1991 Prototype Engineered Barrier System Field Test, Final Rep. UCRL-ID-106159. Lawrence Livermore Nat. Lab.

Scott, R.B. and J. Bonk 1984 Preliminary Geological Map of Yucca Mountain, Nye County, Nevada, with Geologic Sections. USGS-OFR-84-491. Open File Report. U.S. Geol. Survey, Denver, Colo., sib 1986.

Sibson, R.H. 1986 Brecciation processes in fault zones: Inferences from earthquake rupturing. PAGEOPH, 124, 159-175.

Spengler, R.W., C.A. Braun, L.G. Martin and C.W. Weisenberg 1994 The Sundance fault: a newly recognized shear zone at Yucca Mountain, Nevada. Open File Report 94-49 U.S. Geol. Survey, Denver, Colo.

Tsang, Y.W. and K. Pruess 1986 A study of thermally induced convection near a high level nuclear waste repository in partially saturated tuff. LBL-21311. Lawrence Berkeley Laboratory, Berkeley, CA.

Captions to Figures

Figure 1. The computational domain with contours of dimensionless temperature. The top surface is open; there is no flow across the sides or bottom. The repository heat source occupies the middle third of the region and the fault is to the left of center. Contours are isotherms in units ΔT at time $h^2/8\alpha$.

Figure 2. The function $F_1(T)$ of equation (3.12) and (3.13).

Figure 3. Streamline patterns for fault flow numbers between 0.03 and 30; temperature field as in Figure 1a. The streamfunctions are in units of $\{gBkh(\Delta T)/\nu\}\times 10^2$ or $(\alpha Ra)\times 10^2$

Figure 4. (a) Vertical distribution of gas volume flux up the fault in the configuration of Figure 3 as a function of F. The base is at $z/h = 0$, the upper surface $z/h = 1$. Units are $(\alpha Ra)\times 10^2$. (b) The percentage of gas drawn in on the flanks that vents via the fault, as a function of F, in the configuration of Figure 3.

Figure 5. Streamline patterns at $F = 10$ for various fault locations and the temperature field of Figure 1.

Figure 6. Distributions of condensation (solid contours) and evaporation rates (dashed, both x *10*) associated with convective matrix flow at three fault flow numbers. Units are given by (3.11) or (3.13) for convective and diffusive time scales.

Figure 7. Average volume of liquid condensation in a fault (solid lines) per unit area of fault as a function of z/h. Evaporation rates are dashed. Units are $\left(\frac{1}{8}F_1(T)hRa\right)\times 10$.

Figure 8. Contours of $(\nabla\theta)^2$ define the distribution of condensation arising from vapor diffusion.

Figure 9. A cartoon of three-dimensional flow with a fault with $|F \gg 1$ transsecting a repository. The volume fluxes and condensation rates in the fault plane are larger than those in the matrix flow over its entire depth, as indicated on the right, by a factor of order F.

Figure 1

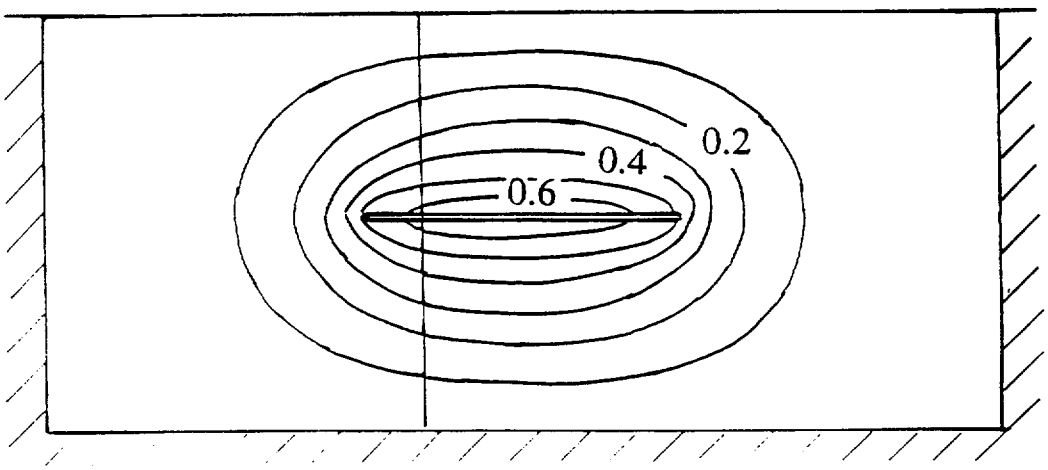

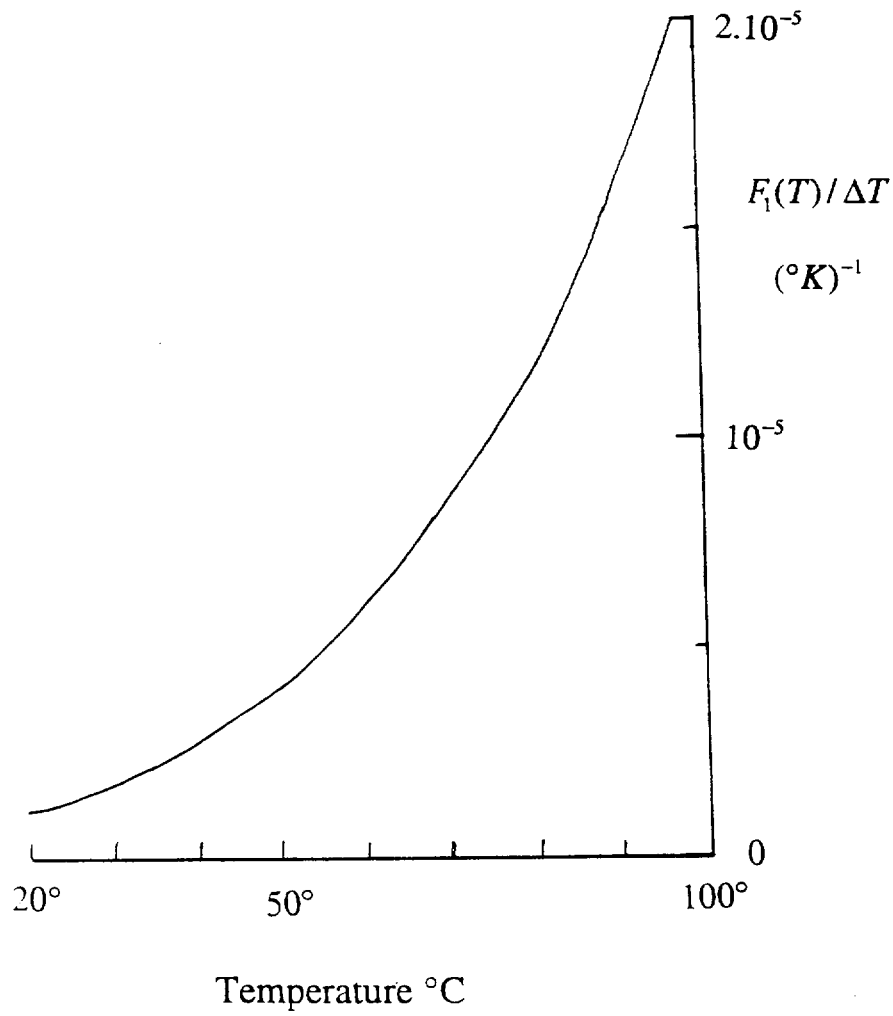

Figure 2

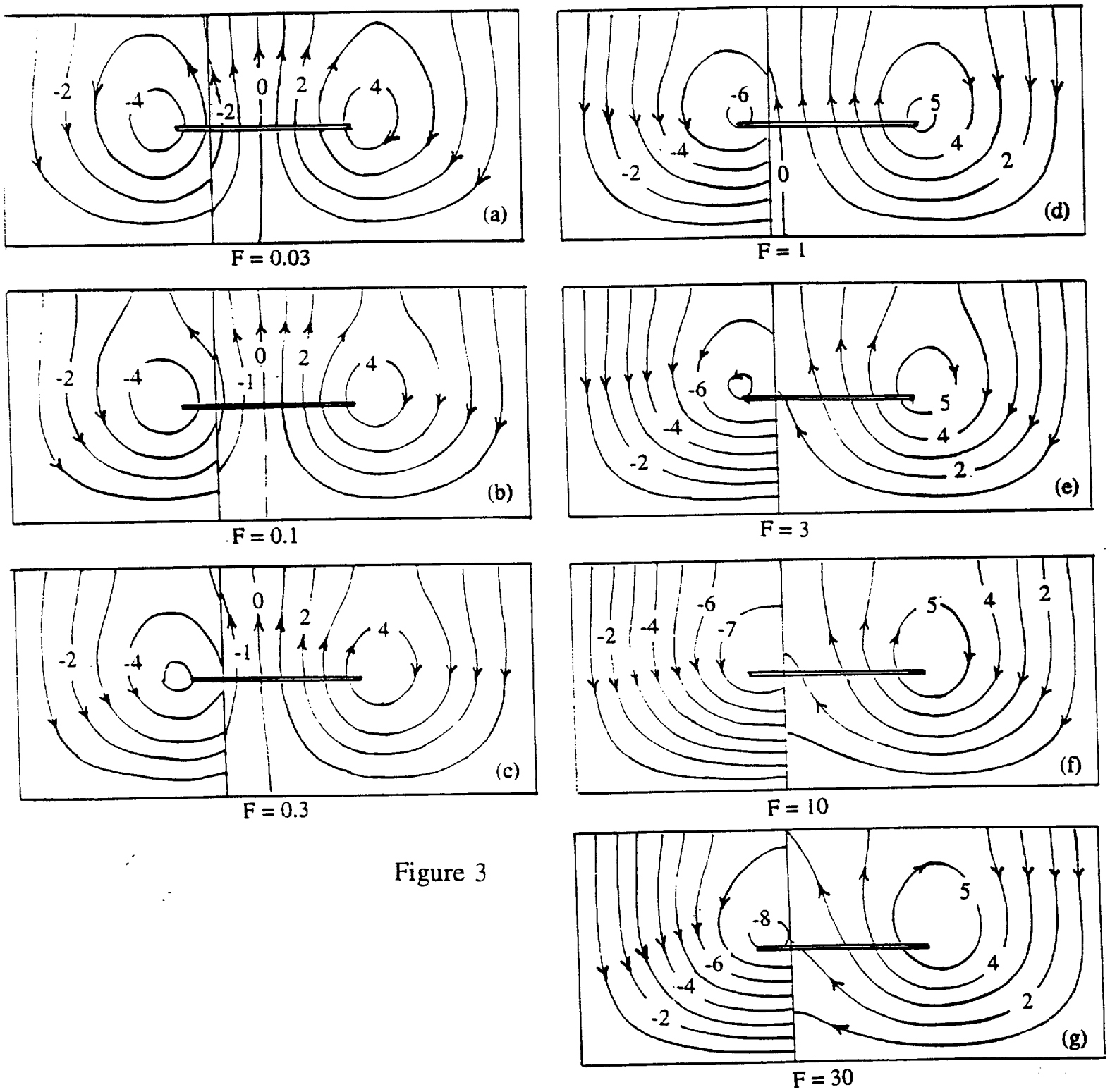
-2
-4
-2
0
2
4
(a)
F = 0.03
-2
-4
0
-1
2
4
(b)
F = 0.1
-2
-4
0
-1
2
4
(c)
F = 0.3
-6
-4
-2
0
5
4
2
(d)
F = 1
-6
-4
-2
5
4
2
(e)
F = 3
-2
-4
-6
-7
5
4
2
(f)
F = 10
-8
-6
-4
-2
5
4
2
(g)
F = 30

Figure 3

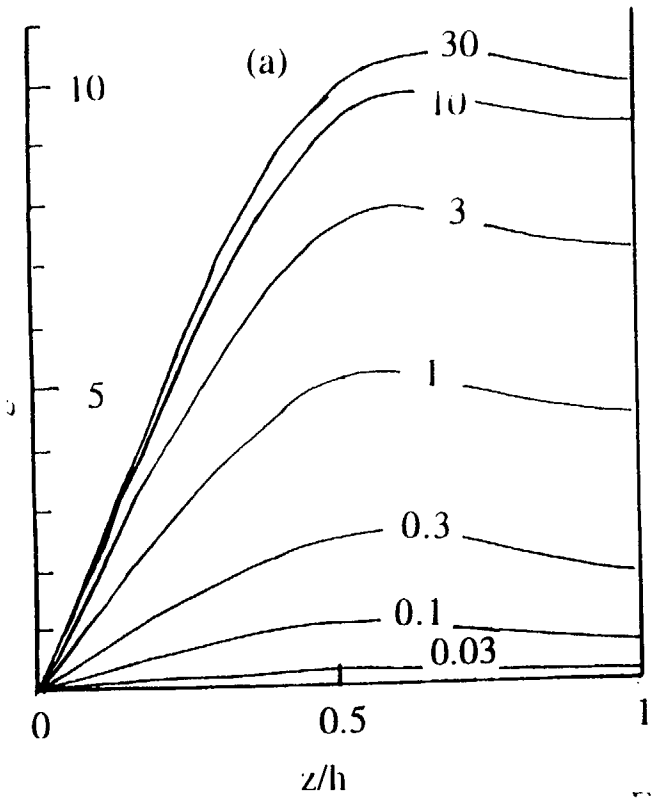
(a)
30
10
3
1
0.3
0.1
0.03
10
5
0
0.5
1
z/h

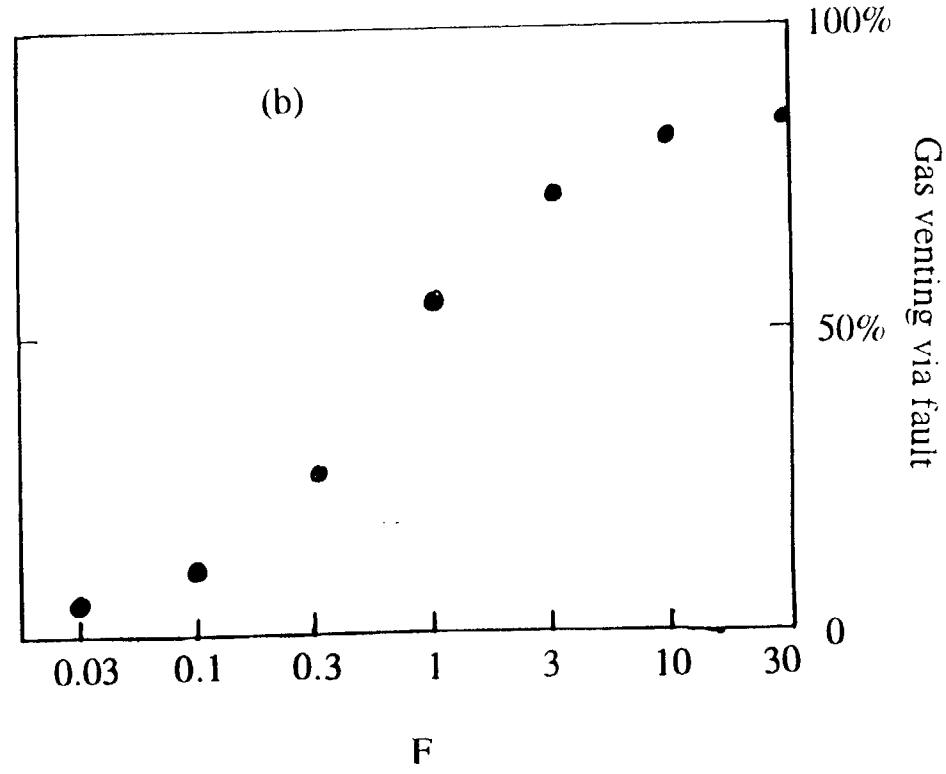
(b)
100%
50%
0
Gas venting via fault
0.03
0.1
0.3
1
3
10
30
F

Figure 5

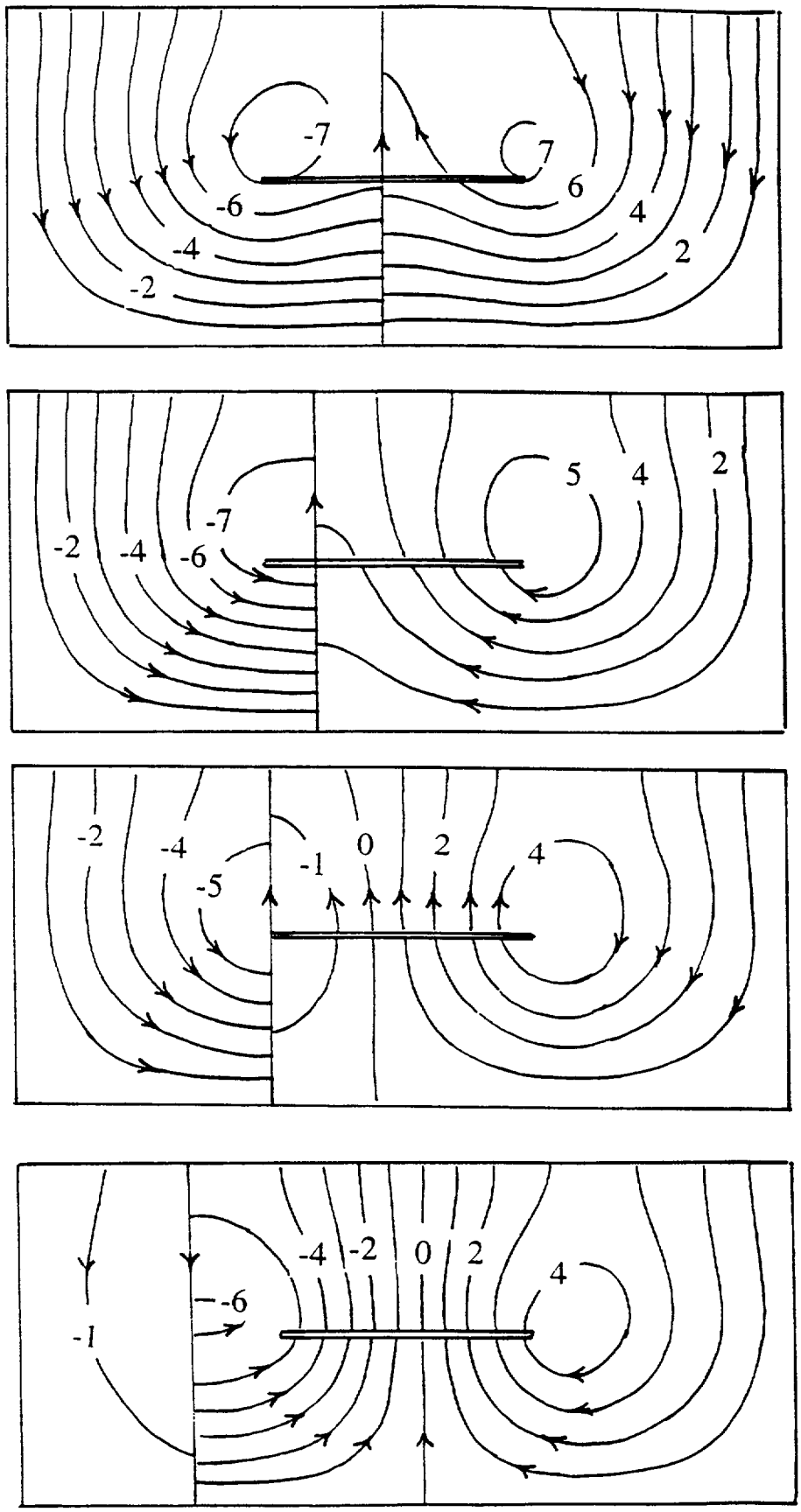

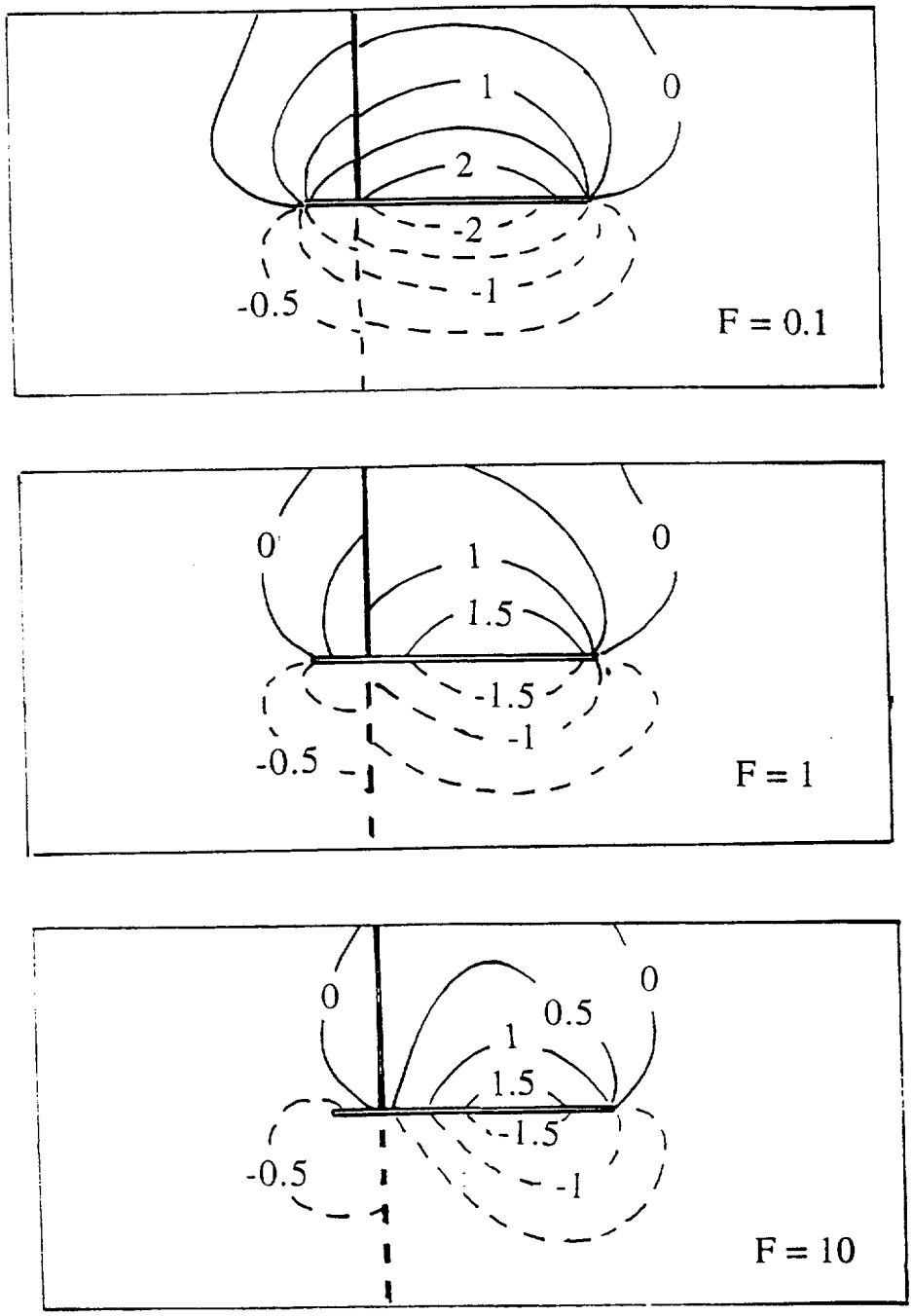

Figure 6

Figure 7

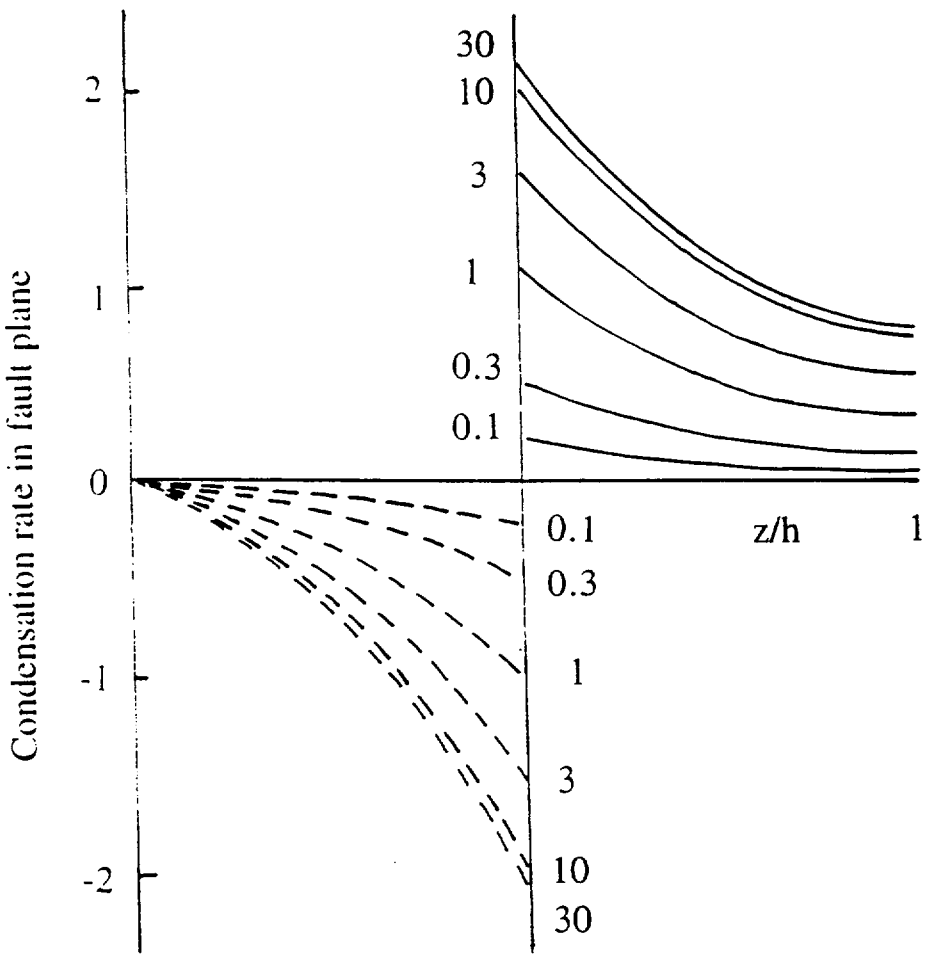
Condensation rate in fault plane
2
1
0
-1
-2
30
10
3
1
0.3
0.1
0.1
0.3
1
3
10
30
z/h
1

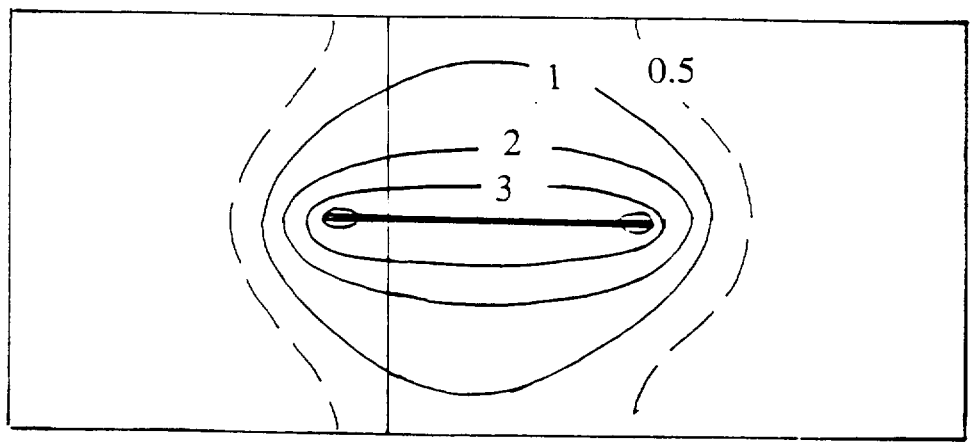

Figure 8

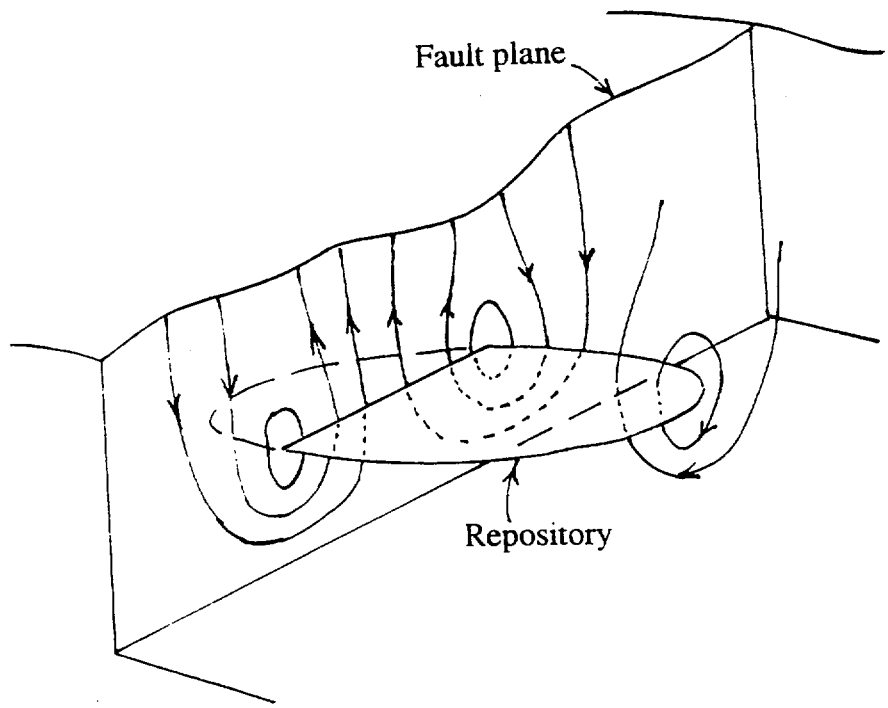

Figure 9